# Active formation of Li-ion batteries and its effect on cycle life

Pathan, Tanveerkhan; Rashid, Muhammad; Walker, Marc; Widanage, W. D. ; Kendrick, Emma

*DOI:*
10.1088/2515-7655/ab2e92

# Active formation of Li-ion batteries and its effect on cycle life

JPhys Energy

PAPER

# Active formation of Li-ion batteries and its effect on cycle life

**Tanveerkhan S Pathan**[1], **Muhammad Rashid**[2], **Marc Walker**[3], **W D Widanage**[2] and **Emma Kendrick**[1,2,4]

[1] School of Metallurgy and Materials, University of Birmingham, Edgbaston, Birmingham B15 2TT, United Kingdom
[2] WMG, University of Warwick, Coventry, CV4 7AL, United Kingdom
[3] Dept of Physics, University of Warwick, Coventry, CV4 7AL, United Kingdom
[4] Dept Of Chemical Engineering, University College London, Torrington Place, London, WC1E 7JE, United Kingdom

**E-mail:** e.kendrick@bham.ac.uk

**Keywords:** formation, SEI, lithium-ion battery, interface, battery manufacutring, Li-ion

Supplementary material for this article is available online

**OPEN ACCESS**

**RECEIVED**
14 April 2019

**REVISED**
24 June 2019

**ACCEPTED FOR PUBLICATION**
2 July 2019

**PUBLISHED**
22 August 2019



## Abstract

The formation of the solid electrolyte interphase during the formation and conditioning steps, is a very time consuming and expensive process. We present an active formation method in $LiNi_{1/3}Mn_{1/3}Co_{1/3}O_2$ (NMC-111) versus graphite lithium-ion batteries, which maintains the cycling performance of the cells. Ten different active formation protocols were evaluated, which consisted of cycling between an upper ($V_u$) and lower ($V_l$) voltages. The cells were evaluated using electrochemical impedance spectroscopy (EIS) and cycling. X-ray photoelectron spectroscopy was used to analyse the surface of the electrodes after cycling. Cycling performance and resistance measurements from the EIS results confirm the different effect of formation protocols in the lifetime and performance of the cells. We show that during the formation protocol the interface composition is optimised through the transport of lithium ions through the initial organic decomposition layer on the graphite at higher cell voltages (>3.65 V). These higher voltage cycling formation protocols giving an interface with greater stability and enhanced cycling are observed in the cells.

## 1. Introduction

Lithium-ion batteries (LIBs) are extensively used as a power source for portable electronic devices and the electrification of the modern transportation sector has driven the growth in demand for LIBs [1–4]. The demand in the automotive sector has been further fuelled by the EU legislation on the mandatory emission reduction targets for new cars [5]. In order to make the electric vehicles and the plug-in hybrid electric vehicles competitive to the automotive industry standard internal combustion engine, the driving range needs to extend beyond 300 miles without increasing the costs significantly [4, 6]; this has led to a noteworthy interest in the research of LIBs. Increasing the energy density of LIBs has been a major focus of recent research, with many scientists developing and improving cathode materials (e.g. higher nickel content) and anode materials (e.g. silicon or tin composites) for high-voltage and high-energy LIBs [7]. However, in addition to the materials development, significant research and development is also required into current and future manufacturing methods for batteries, to improve and optimise the cell designs and lower the costs in manufacturing [6, 8–13].

Current manufacturing processes are based upon the methods developed by Sony in the 1990s [14]. The multi-step process of LIB manufacture is illustrated in figure 1. The active materials are first mixed with a binder and conductive additive in a solvent to prepare an ink. The rheology of the ink is optimised for the coating process, and for high-energy electrodes, this is performed on a slot die or comma bar coater. The ink needs to flow when a shear force is applied and stop when the force is removed. Once the ink is deposited on the current collector, the electrode is dried and then calendared. This process creates and optimises the porosity and the electronic conductive pathways. The electrodes are then cut and assembled into stacks or wound cells. Tags are welded onto the ends of the cathode and anode stacks or rolls, and then the stack is placed into a container. For

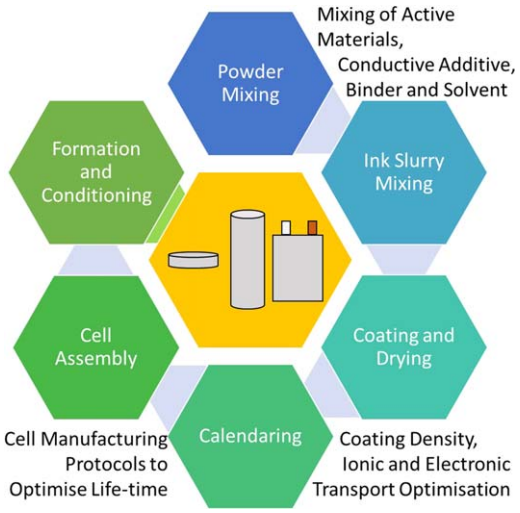


**Figure 1.** Standard manufacturing process diagram for LIBs.

pouch cells the electrolyte is injected into the pouch, and the pouch is evacuated and the electrolyte displaces the air in the pores of the electrode. After filling, the cells are sealed and then undergo a formation process.

Besides the raw material cost, cell formation is the most expensive step in battery manufacturing, accounting for about 6% of the total pack cost [6, 9, 15]. As reported by Wood *et al* [15], the formation and conditioning steps are time consuming and expensive processes that are done at very low charge/discharge rates. This process may take between 1.5–4 weeks, with different charging voltages, rest steps and degassing stages. These steps are optimised by the battery manufacturer for each cell chemistry and cell format. This formation and conditioning (or ageing) step requires electrochemical battery cyclers, environmental chambers for the conditioning steps, and degassing stations, all of which add expense with regard to equipment and utilised floor space [2, 14].

The formation process is the step during which the surface interfaces are grown to stabilise the electrolyte against the lithiated graphite. The electrolyte decomposes upon the surface of the fresh graphite anode and this results in the formation of the solid electrolyte interface (SEI) layer. This is a passivation layer, which is electrically resistive but conductive to the Li ions [16–18]. The SEI layer acts as a protective layer to prevent continuous electrolyte decomposition and solvent co-intercalation into graphitic layers during subsequent cycles [6, 19]. With an imperfect SEI layer, subsequent graphite exposure results in further electrolyte decomposition and SEI growth [20–22]. Furthermore, the nature and behaviour of the SEI layer affects the performance of the cell and safety [7, 23]. The cell formation protocol is essential to create a stable SEI layer and minimise active lithium loss, electrolyte depletion and capacity fade over the lifetime of the battery [2, 6]. In recent times, a great deal of research has been carried out to understand the formation and electrochemistry of the SEI through combined atomic-scale microscopy and *in situ* and operando techniques, scanning electrochemical microscopy and neutron scattering techniques [24–26]. An ideal SEI layer would be electrically resistive and highly permeable to lithium ions, close to few nanometres thick with tolerance to expansion and contraction that would take place on the anode surface during charge/discharge cycles. It should be insoluble in the electrolyte and stable over a wide range of temperatures and voltages. The factors that affect the properties of the SEI layer are depicted in figure 2 [17, 27].

Here, we present research into a faster 'active formation' process, rather than current passive formation and conditioning and show that the composition of the SEI has a significant affect upon its resistance, growth and hence the lifetime of a lithium-ion cell, compared to a baseline formation. The cell chemistry utilised in this work is $LiNi_{1/3}Mn_{1/3}Co_{1/3}O_2$ (NMC-111) versus graphite.

## 2. Methodology and experiments

### 2.1. Material information

*2.1.1. Coin cell constituents*

CR2032 coin cell kits (Hohsen Corp., Japan) were used to assemble the coin cells (20 mm diameter and 3.2 mm height). The kit comprised an SS (stainless steel 316L) cap, aluminium cladded SS case (in the case of cathode half cells and full cells) and SS case (in the case of anode half cells) with a polypropylene gasket, SS disk spacers and SS wave washer.

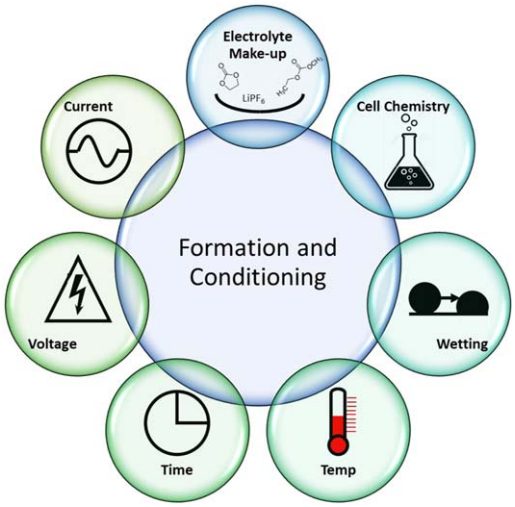


**Figure 2.** Factors affecting the formation of the SEI layer [17].

*2.1.2. Electrodes*

The graphite anode consisted of 91.83%wt. graphite (Superior Graphite) as the active material and 6.00%wt. polyvinylidene difluoride (PVDF) binder (Solef® 5130, Solvay), 2.00%wt. carbon C65 (Timcal) and 0.17%wt. oxalic acid (Sigma Aldrich). The NMC cathode coating formulation used was 92.00%wt. NMC-111 (BASF), 3.00%wt. PVDF binder and 3.00%wt. C65 (Timcal) and 2.00%wt. KS 6L as conductive binders. The formulation was mixed into a slurry using a Thinky ARE 250 centrifugal mixer (Thinky, USA). The slurry was then coated onto the copper (for the anode) and aluminium (for the cathode) foils using a draw-down coater (K Paint Applicator, RK Printcoat Instruments, UK) with a doctor blade and the electrodes were dried on a hot plate at 90 °C. Following the drying step, the electrodes were dried overnight under dynamic vacuum at 50 °C. Then, 15.0 mm discs in the case of the anode and 14.8 mm discs in the case of cathode were cut out from the electrode sheets. In the case of half cells, lithium metal discs were used as counter electrodes.

*2.1.3. Electrolyte*

The electrolyte used was PuriEL Battery Electrolyte (R&D 281) from Soulbrain (Michigan, USA). The composition of the electrolyte was 1.0 M $LiPF_6$ in EC/EMC (ethylene carbonate/ethyl methyl carbonate) $= 3/7$ (v/v) $+$ 1%wt. VC (vinylene carbonate). Each coin cell was filled with 60 $\mu$l of electrolyte.

*2.1.4. Separator*

19 mm diameter discs were cut out from a sheet of the three-layer (polypropylene—polyethylene—polypropylene) Celgard® 2325–1850M—BM68 separator.

**2.2. Coin cell assembly**

In order to assemble the coin cells, the electrodes were weighed first and subsequently, the anodes and cathodes were paired to achieve a capacity ratio of 1.1 for the anode/cathode. The coin cells were assembled using the parts discussed earlier and a schematic of the coin cell assembly is depicted in figure 3. The coin cells were then sealed using a hydraulic crimper (MSK-110, MTI Corporation, USA).

**2.3. Electrochemical test protocols**

*2.3.1. Formation method*

The cells were assembled and soaked, and then a formation step was performed at C/20, between two voltage limits, $V_u$ (upper voltage) and $V_l$ (lower voltage) for ten cycles. In the first case, the cells were charged to 4.0 V ($V_u$) and then discharged to 2.6 V ($V_l$). In subsequent cases, different voltage windows were chosen, as shown in table 1. Three cells were used for each case in order to obtain standard deviations. The formation time for each case along with the voltage profiles are shown in figure 4. After the formation step, all the cells were discharged to 2.5 V and a potentiostatic electrochemical impedance spectra scan was obtained and the cells were then cycled for 500 cycles. As a control scenario, three cells were cycled directly without any prior formation step.

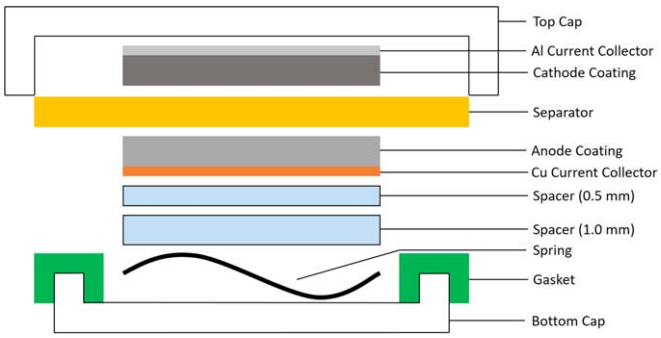


**Figure 3.** Schematic of the coin cell parts used for assembling CR2032 coin cells.

**Table 1.** Upper voltage ($V_u$) and the lower voltage ($V_l$) limits used for the ten different formation cases.

| Case number | Upper voltage, $V_u$ (V) | Lower voltage, $V_l$ (V) |
|---|---|---|
| 1 | 4.0 | 2.6 |
| 2 | 4.0 | 3.65 |
| 3 | 3.65 | 3.3 |
| 4 | 3.3 | 2.95 |
| 5 | 2.95 | 2.6 |
| 6 | 4.0 | 2.95 |
| 7 | 3.65 | 2.6 |
| 8 | 4.0 | 3.3 |
| 9 | 3.65 | 2.95 |
| 10 | 3.3 | 2.6 |

*2.3.2. EIS and cycling*

The electrochemical performance of the coin cells was tested using the BCS 805 battery cyclers (Bio-Logic Science Instruments, France). The cells were tested for 500 cycles with EIS scan obtained after formation and at every 50, 100, 200 and 500 cycles for all cells. For the EIS scan, the frequency range used was 20 mHz–10 kHz. This range was limited by the equipment, and the amplitude was 10 mV around the open circuit potential. The cells were cycled between 4.2–2.5 V at a rate of C/2 with CC_CV/CC (constant current charge, constant voltage and constant current discharge). For the CV step, the cells were held at 4.2 V until the current decayed to 10% of the originally applied current in the CC step. A sample V + I versus t curve is shown in figure 5.

*2.3.3. Half-cell tests*

Anode and cathode half cells were made in order to calculate the capacities of the anode and cathode. In the case of cathode half cells, two cycles at C/20 were performed with CC_CV/CC steps between 4.2–2.5 the V. In case of the anode half cells, the cells were discharged first to 0.05 V and then charged back to 1.5 V at C/20 using CC_CV/CC steps.

*2.3.4. Surface characterisation*

The x-ray photoelectron spectroscopy (XPS) data were obtained using a Kratos Axis Ultra DLD spectrometer. The cycled cells were disassembled in an inert glove box (argon) and the samples were then mounted onto a copper stub using electrically conductive carbon tape. Samples were transferred to the spectrometer under an argon atmosphere using a sealed vacuum transfer unit, with the transfer chamber of the spectrometer vented to Ar in order to prevent exposure of the surface to air. XPS measurements were performed at room temperature using a monochromated Al K$\alpha$ x-ray source and at a take-off angle of 90° with respect to the surface parallel. The core level spectra were recorded using a pass energy of 20 eV (resolution approx. 0.4 eV), from an analysis area of 300 $\times$ 700 $\mu$m. The surfaces of the samples were found to positively charge under the x-ray beam during the experiments and to compensate for this, the surfaces were flooded with a beam of low-energy electrons during data acquisition. This in turn required subsequent re-referencing of the XP spectra, using the graphitic component of the C1s region at 284.3 eV as the reference point. The spectrometer work function and binding energy scale were calibrated using the Fermi edge and 3d {5/2} peak recorded from a polycrystalline Ag sample prior to the commencement of the experiments. The data were analysed with the CasaXPS software package,

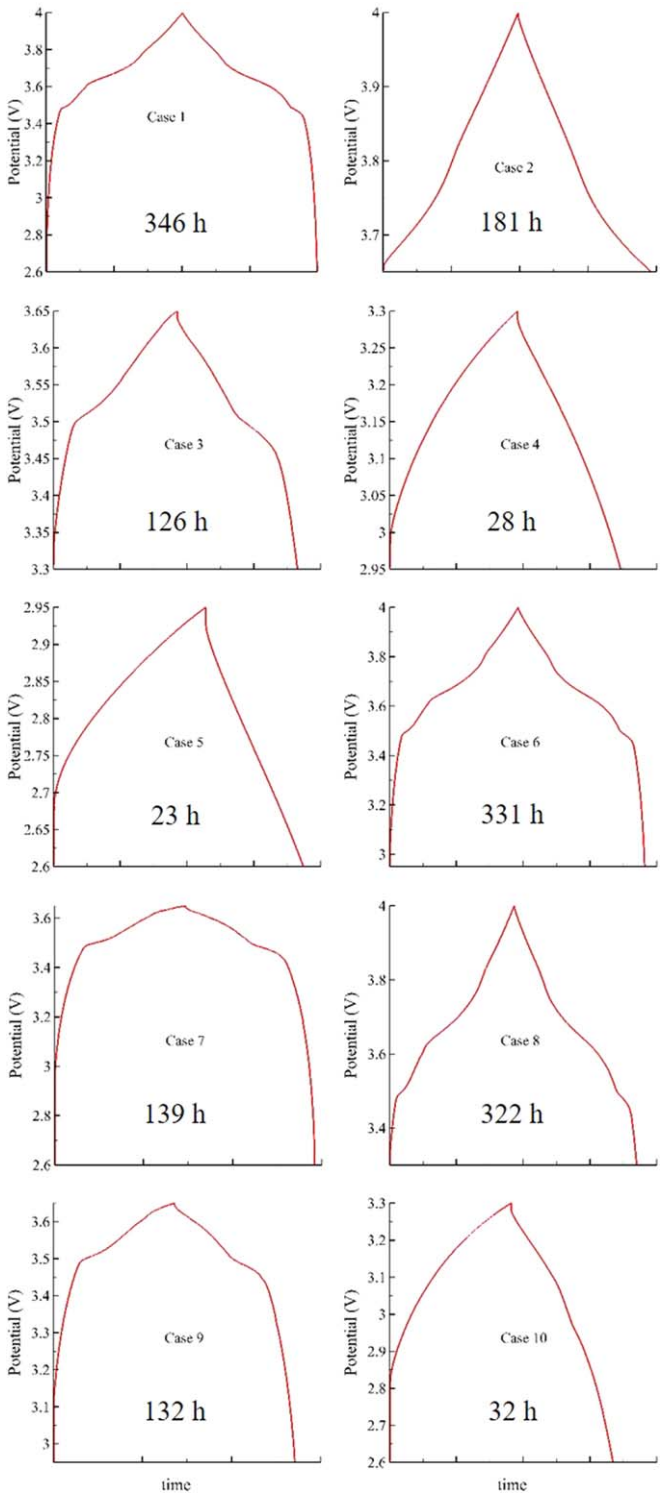


**Figure 4.** Voltage profiles for the ten different formation cases with the formation time in hours.

using Shirley backgrounds and mixed Gaussian–Lorentzian (Voigt) line shapes and asymmetry parameters where appropriate. The elemental peaks were identified and assigned to different bonding environments using the handbook of XPS [28].

## 3. Results and discussion

The formation method chosen in this work was aimed at probing the anodic interface and the formation of the most stable interface layer. An irreversible capacity loss can be seen between 1.25–0.5 V versus $Li/Li^+$ on the graphite anode and this process is observed between 2.25–3 V in a full-cell configuration and is assumed to be

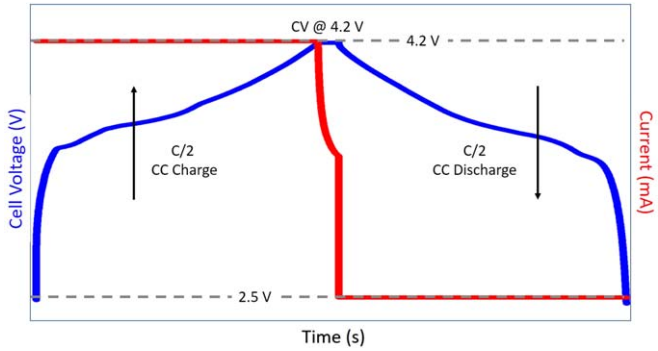


**Figure 5.** Sample voltage and current versus time curve for a C/2 CC_CV/CC charge-discharge of a coin cell.

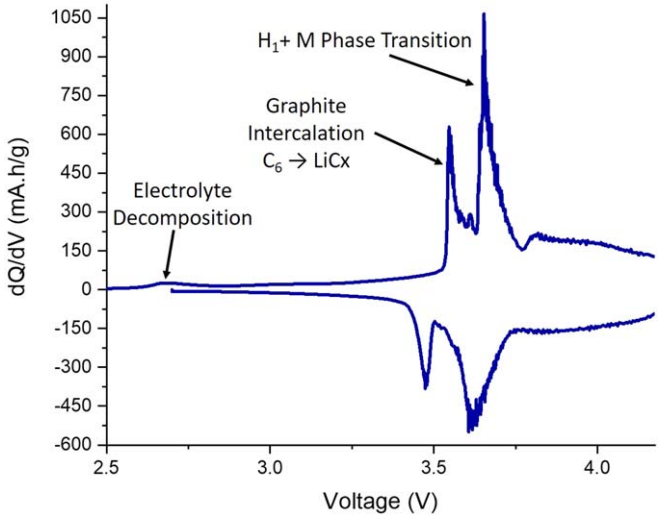


**Figure 6.** Example of first-cycle dQ/dV versus V plot for a typical NMC-111 versus graphite coin cell.

the decomposition of the electrolyte components [29]. This can be seen in the dQ/dV versus V plot (figure 6) of a full cell at ~2.6 V. The peaks at 3.5 and 3.6 V upon charge relate to the crystal structure changes in the graphite $C_6 \rightarrow LiC_x$ and $H_1$-M phase change in the NMC, respectively. On the first charge/discharge of the cell, there is a loss in capacity known as the 'irreversible capacity loss', which is mainly needed to form the SEI layer. (This can be seen in the dQ versus V (versus $Li/Li^+$) plot in figure S.1, available online at stacks.iop.org/JPENERGY/1/044003/mmedia in the supplementary information.)

In order to probe the electrochemical formation of the SEI layer, several voltage windows were chosen for which the anodic voltage was near (0 V versus $Li/Li^+$) and the cathodic cell voltage was low enough to reduce the high-voltage stress on the cathode (figure 7). Hence, 4.0 V was chosen as the highest cell voltage for the formation step. This allowed the anodic interface formation to be probed, whilst assuming that the cathode was not stressed at the high voltages and the formation of a cathode electrolyte interphase (CEI) layer was assumed to be limited. Our aim was to probe the anodic SEI layer formation rather than the cathodic one. Post formation cell cycling was done between 4.2–2.5 V, as this is typical for this cell chemistry, to see if the anodic SEI formation could be improved for the cell.

### 3.1. Electrochemical impedance spectroscopy (EIS) results

The experimental data for the EIS scans were fitted using the equivalent circuit model shown in figure 8. The high-frequency intercept with the real axis reflect the ohmic resistance or the series resistance (represented as $R_S$), that results from the electron transport through the general electrical set-up such as current collectors, cables and leads [2, 30]. The first semi-circle in the high to medium frequency range could be attributed to the lithium-ion migration through the surface films, i.e. the SEI layer (represented as $R_{SEI}$). The second semi-circle in the medium to low-frequency range would be related to the charge transfer resistance (represented as $R_{CT}$) arising from the charge transfer between the electrolyte and the solid surfaces [31]. The linear Warburg element

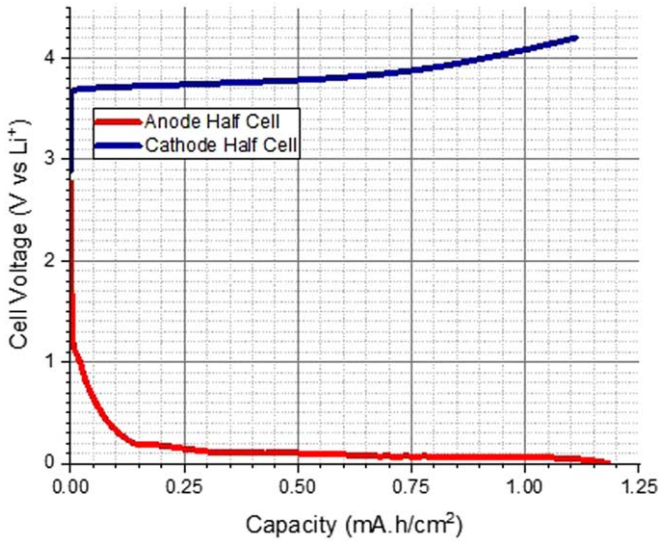


**Figure 7.** Voltage versus capacity plot for anode and cathode half cells whilst charging.

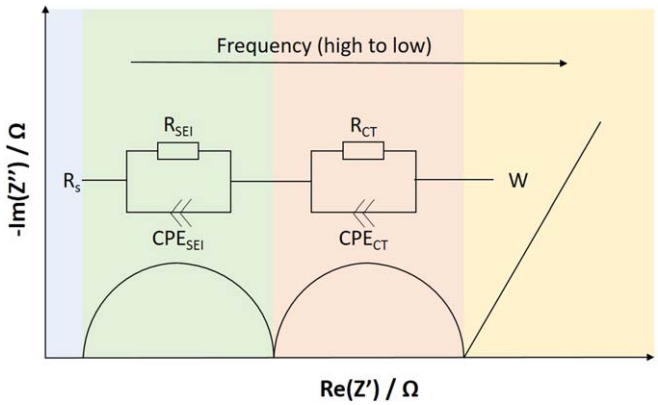


**Figure 8.** Equivalent circuit model used in the impedance analysis.

at the low-frequency range corresponds to the lithium-ion diffusion through the active material. The resistance arising from the transport of lithium ion through the surface films is assigned as the resistance from the interfaces that are developed as a result of the formation of an SEI layer in the battery.

Figure 9 shows an example of the Nyquist and Bode plots for the experimental and the fitted data acquired immediately after formation for a case 2 (4–3.65 V) cell.

As a general trend, the SEI layer resistance and the charge transfer resistance increases with increasing number of cycles in all cases, as can be seen in table 2 (figures S.2 and S.3 in supplementary information). As expected, the maximum increase in the SEI resistance was seen in the three cells that were cycled without any formation prior to cycling. The standard case 1 where the cells were formed between 4.0–2.6 V also showed an increase in the resistance after formation to resistance after 500 cycles. Case 2 (2.4–3.65 V), case 8 (4.0–3.3 V) and case 9 (3.65–2.95 V) showed similar increase in the resistance values with cycling; with case 2 showing the least increase in the resistance after 500 cycles. Figure 10 shows the comparison between the EIS scans for case 1, case 2 and no formation cells, and table 2 shows the increase in the resistance values for all the cells after formation, and after 50, 100, 200 and 500 cycles. Steady resistance values and minimal increase after cycling would suggest the presence of an SEI layer that would remain constant and not degrade with cycling.

### *3.1.1. Cycle life*

Cycle life of LIBs is a key testing parameter in terms of their performance. As expected, the cells that were not formed prior to cycling performed poorly and 80% of the original capacity was reached after only 244 cycles, and after 500 cycles, only 48% capacity was retained (figure 11). For the standard case 1, 80% capacity was reached after 337 cycles and about 60% was retained after 500 cycles.

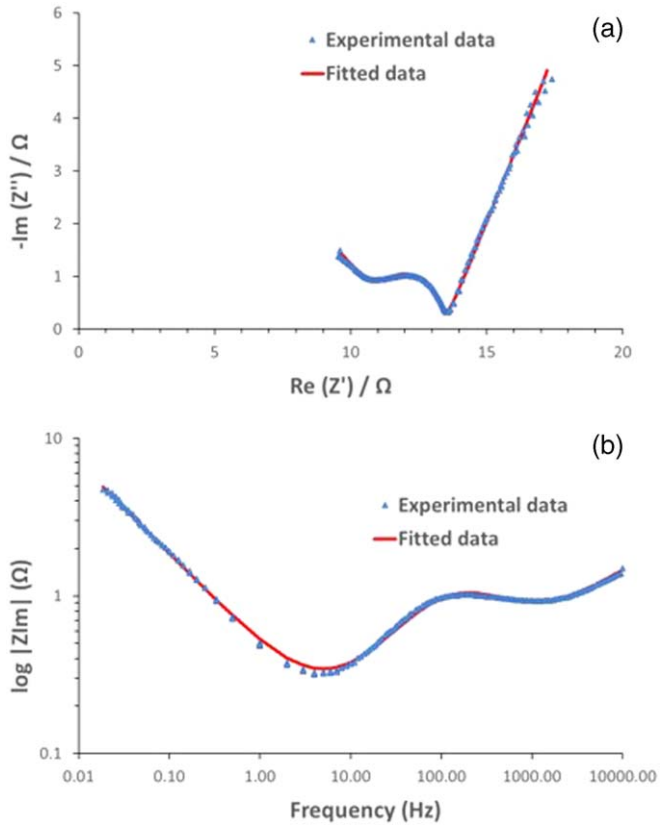


**Figure 9.** Experimental and fitted data for the EIS scan obtained immediately after formation for a case 2 (4–3.65 V) cell; (a) Nyquist plot and (b) Bode plot.

**Table 2.** Increase in the SEI resistance values for all different cases at various stages during their cycling.

| Case number | Vu (V) | Vl (V) | After formation (Ohm) | 50 cycles (Ohm) | 100 cycles (Ohm) | 200 cycles (Ohm) | 500 cycles (Ohm) | Increase after 500 cycles (Ohm) |
|---|---|---|---|---|---|---|---|---|
| 1 | 4 | 2.6 | 8.910 | 9.053 | 9.839 | 11.606 | 12.900 | 3.990 |
| 2 | 4 | 3.65 | 11.254 | 11.659 | 11.907 | 12.488 | 13.964 | 2.710 |
| 3 | 3.65 | 3.3 | 9.205 | 9.018 | 9.766 | 10.672 | 15.293 | 6.088 |
| 4 | 3.3 | 2.95 | 7.723 | 7.069 | 8.814 | 10.531 | 15.084 | 7.361 |
| 5 | 2.95 | 2.6 | 8.627 | 9.334 | 10.027 | 11.178 | 14.706 | 6.079 |
| 6 | 4 | 2.95 | 7.284 | 7.707 | 7.890 | 9.252 | 11.674 | 4.390 |
| 7 | 3.65 | 2.6 | 9.695 | 8.975 | 9.061 | 9.936 | 14.253 | 4.558 |
| 8 | 4 | 3.3 | 7.118 | 7.579 | 7.682 | 8.302 | 10.502 | 3.384 |
| 9 | 3.65 | 2.95 | 7.068 | 7.940 | 8.191 | 8.077 | 10.024 | 2.956 |
| 10 | 3.3 | 2.6 | 8.852 | 8.508 | 9.555 | 9.979 | 14.000 | 5.148 |
| No formation | | | 7.930 | 8.776 | 9.996 | 11.922 | 18.500 | 10.570 |

The best performance was obtained from case 2, where almost 86% of the capacity was retained after 500 cycles where formation was performed between 3.65–4 V. Cases 8 and 9 also performed well and reached 80% capacity after 496 and 413 cycles, respectively. After 500 cycles, almost 80% capacity was retained for the case 8 cells and just above 75% capacity was retained for case 9 cells. Case 5 had reasonable performance with 75% capacity retained after 500 cycles, with 457 cycles taken to reach 80% capacity. Cases 6 and 7 performed almost equally with 69% and 72% capacities retained after 500 cycles. Case 10 cells did not perform well and had a constant decline in capacity with 80% capacity reached after 306 cycles and only 64% retained after 500 cycles. Cases 3 and 4 depicted similar performances with 80% capacity reached within less than 400 cycles and about 66% capacity retained after 500 cycles. It can be observed that the higher $V_u$ (4 V) utilised during the formation cycling produces cells with better capacity retention. A higher $V_L$ and hence a smaller formation voltage window ($V_U$-$V_L$) is observed to improve the cycling perofrmance (figure 12) and this is also attributed to a lower impedance or resistance of the SEI layer (figure 13). This improved performance can be attributed to an interface

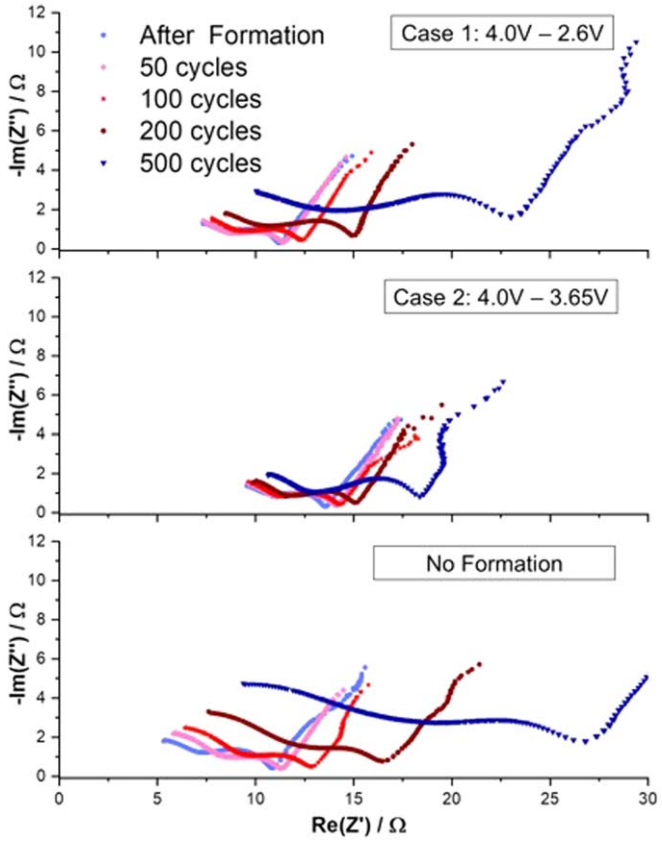


**Figure 10.** EIS scans for case 1 (standard formation), case 2 (2.4–3.65 V) and no formation at various stages during their cycling.

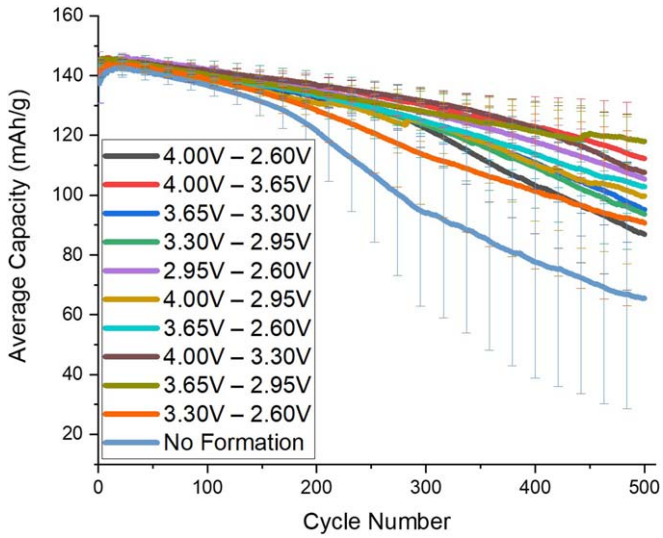


**Figure 11.** Average capacity versus cycle number for all different cases.

with greater stability and lower resistances. Improved cycling is observed in cases 2 and 8 where $V_U$ is 4 V and $V_L$ is 3.65 and 3.3 V, respectively.

Table 3 describes the capacity retained after 500 cycles and number of cycles after which 80% capacity was reached for all the cases.

### 3.2. Post cycling surface analysis

Based on the results from the EIS scans and the cycling data, a coin cell from the standard formation protocol (case 1) and a cell from the best performing protocol (case 2) were de-crimped and disassembled for further

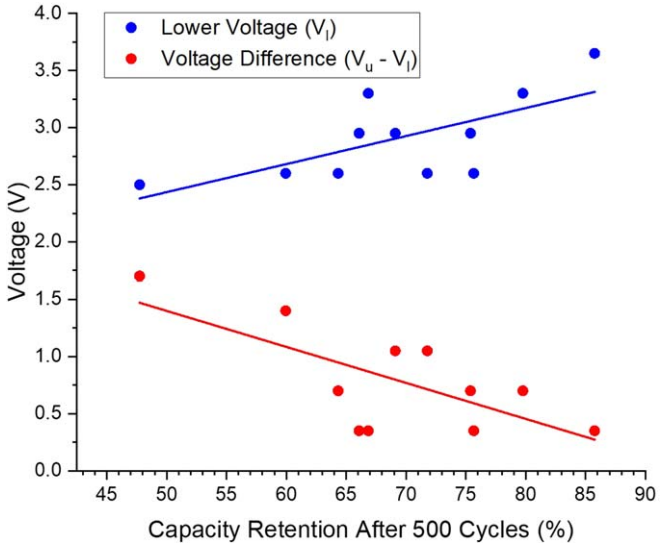


**Figure 12.** Change in % capacity retention after 500 cycles with respect to the lower voltage cut-off and the voltage cycling window during formation.

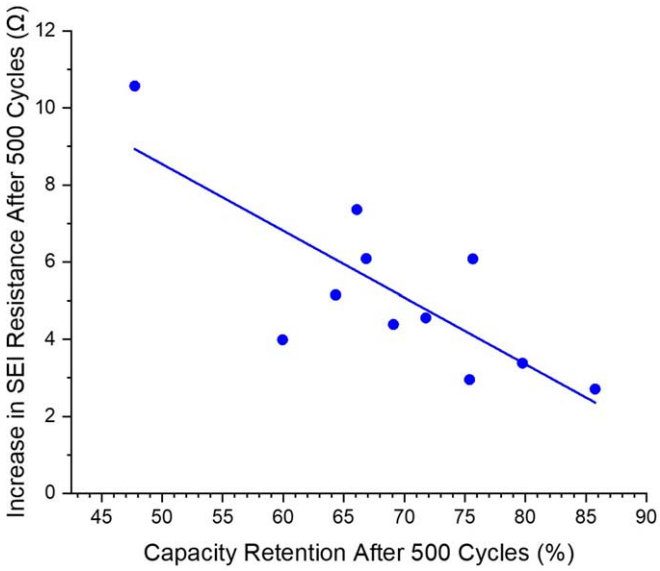


**Figure 13.** Increase in the SEI resistance of the cells after 500 cycles versus the % capacity retention of the cells.

**Table 3.** Capacity retention after 500 cycles and number of cycles (N) for reaching 80% capacity for all different cases.

| Case number | $V_u$ (V) | $V_l$ (V) | Retention (%) | N at 80% |
|---|---|---|---|---|
| 1 | 4 | 2.6 | 59.95% | 337 |
| 2 | 4 | 3.65 | 85.76% | >500 |
| 3 | 3.65 | 3.3 | 66.85% | 382 |
| 4 | 3.3 | 2.95 | 66.08% | 369 |
| 5 | 2.95 | 2.6 | 75.66% | 457 |
| 6 | 4 | 2.95 | 69.10% | 373 |
| 7 | 3.65 | 2.6 | 71.78% | 397 |
| 8 | 4 | 3.3 | 79.76% | 496 |
| 9 | 3.65 | 2.95 | 75.39% | 413 |
| 10 | 3.3 | 2.6 | 64.33% | 306 |
| 0 | No formation | | 47.74% | 244 |

**Table 4.** Elemental composition with bonding (in percentage) for anodes obtained from XPS analysis for the fresh, and after 500 cycles for the standard formation and case 2 (4–3.65 V) anodes.

| Element | Fluorine | | | Oxygen O1s | | | | Carbon C 1s | | | | | | | | Lithium 1s | | Silicon 2p | | Phosphorous 2p | | | | Sulphur 2p | | | |
|---|---|---|---|---|---|---|---|---|---|---|---|---|---|---|---|---|---|---|---|---|---|---|---|---|---|---|---|
| Bonding | LiPF6+(-CH2-CF2-)n | (-CF2-CF2-)n | SF6 | O-(C=O)-C | C-O-C (Aliphatic) | O-(C=O)-C (Aliphatic) | H2O | Graphitic C-C | Pi-Pi* | sp3 (C-C, C-H) | C-O | C=O | O=C-O | CO3 | CF2-CH2 | CF2-CF2 | LiF | LiPF6 | Si 2p3/2 | Si 2p1/2 | P 2p3/2: PO3 | P 2p1/2: PO3 | P 2p3/2 | P 2p1/2 | S 2p3/2: Li2SO4 | S 2p1/2: Li2SO4 | S 2p 3/2: $SF_6$ | S 2p1/2: $SF_6$ |
| Fresh Anode | 17.85 (-CH2-CF2-)n | 3.46 | - | 0.90 | 1.15 | 0.38 | 0.06 | 49.16 | 2.47 | - | 9.63 | 5.95 | 0.98 | - | 7.99 | - | - | - | - | - | - | - | - | - | - | - | - | - |
| Standard Formation Anode | 11.77 | 7.03 | 0.92 | 2.18 | 12.25 | 3.42 | 2.42 | 4.39 | 0.22 | 2.06 | 12.17 | 2.65 | 3.19 | 1.81 | 2.80 | 0.63 | 23.39 | 1.09 | 0.47 | 0.46 | 1.41 | 1.39 | 0.63 | 0.61 | 0.08 | 0.08 | 0.25 | 0.24 |
| Case 2 (4 – 3.65 V) Anode | 17.75 | 6.58 | 1.02 | 0.59 | 1.65 | 7.43 | 2.24 | 1.48 | 0.07 | 0.67 | 16.35 | 4.06 | 2.16 | 1.02 | 1.54 | 0.72 | 29.25 | 1.42 | 0.01 | 0.01 | 1.14 | 1.11 | 0.48 | 0.47 | - | - | 0.31 | 0.31 |

analysis of the electrodes post cycling. In addition to these two, a fresh pair of anode and cathode were also analysed using XPS and SEM.

### *3.2.1. XPS analysis*

#### *3.2.1.1. Anodes*

The XPS spectra of the anodes depict typical behaviour of PVDF-based graphite anodes with carbon, fluorine and oxygen being the key elements in the spectra. Different bonding environments arising from the different electrolyte decomposition products present in the cycled anodes with C–O, C=O, –O–C=O, C–O–C, –O–(C=O)–C bonding environments present in the oxygen and carbon spectra arising from the decomposition of EC [$(CH_2O)_2CO$] and EMC [$C_2H_5$–O–CO–O–$CH_3$]. In addition to these, the cycled anodes show lithium and phosphorous. Trace amounts of sulphur and silicon were detected on the cycled anodes, most likely due to contamination (figures S.4–S.6 in supplementary information). Table 4 shows the elemental composition in atomic percentage for all the elements and their bonding present in a fresh anode sample, the standard formation sample and the case 2 (4.00–3.65 V) sample after 500 cycles.

In the case of the fresh anode, a typical PVDF-based anode can be seen with about 76% of the total surface being carbon. Within the carbon, almost 65% of the total carbon is graphitic in nature at 284.3 eV and 10% resulting from the fluorocarbon environments in PVDF at ~291 eV. The remaining carbon was present as various single and double C–O bonds. After cycling for 500 cycles (figure 14), the graphite peak intensity decreases, while the $sp^3$ carbon intensities are seen at ~284.8 eV (C–C/C–H), suggesting the nonconductive species from the EMC component of the electrolyte. Along with the presence of $sp^3$ carbon, the cycled anodes show a small shift in the binding energies of the carbon components, in particular the C–O component. This was likely due to a change in the specific types of C–O–H or C–O–C environments present on the surface; a result of the likely complex decomposition mechanisms of both EC and EMC. In light of this, it would therefore be expected that the C–O peak shifts slightly to higher binding energies. There could also be a small degree of uncertainty with the energy referencing due to changes in the surface potential as the composition of the surface alters, which may influence the binding energy of each component in the spectrum.

Furthermore, a significant increase in the C–O bonding is seen in the cycled anodes, most likely from the solvent degradation resulting in the opening of the EC ring and from C–O bonding in EMC. The key difference in the two cycled anodes is the presence of carbonates; most likely to be lithium carbonates, present as a result of solvent reduction and subsequent lithiation; with more carbonates on the case 1 standard formation anode at 6% of total carbon as opposed to 3.6% in the case of the better performing case 2 (4–3.65 V) anode.

The fluorine XPS analysis of both the cycled anodes reveals the presence of lithium, and phosphorous ($LiPF_6$) bonding for fluorine (figures 15(b) and (c)) that was not seen in the fresh anodes (figure 15(a)). All of these elements and the $LiPF_6$ can be attributed to the electrolyte salt. However, there was no apparent LiF content in this layer. Another aspect is that the PVDF ($CF_2$-$CH_2$) is further fluorinated in the cycled electrodes and is present as $(CF_2$-$CF_2)_n$.

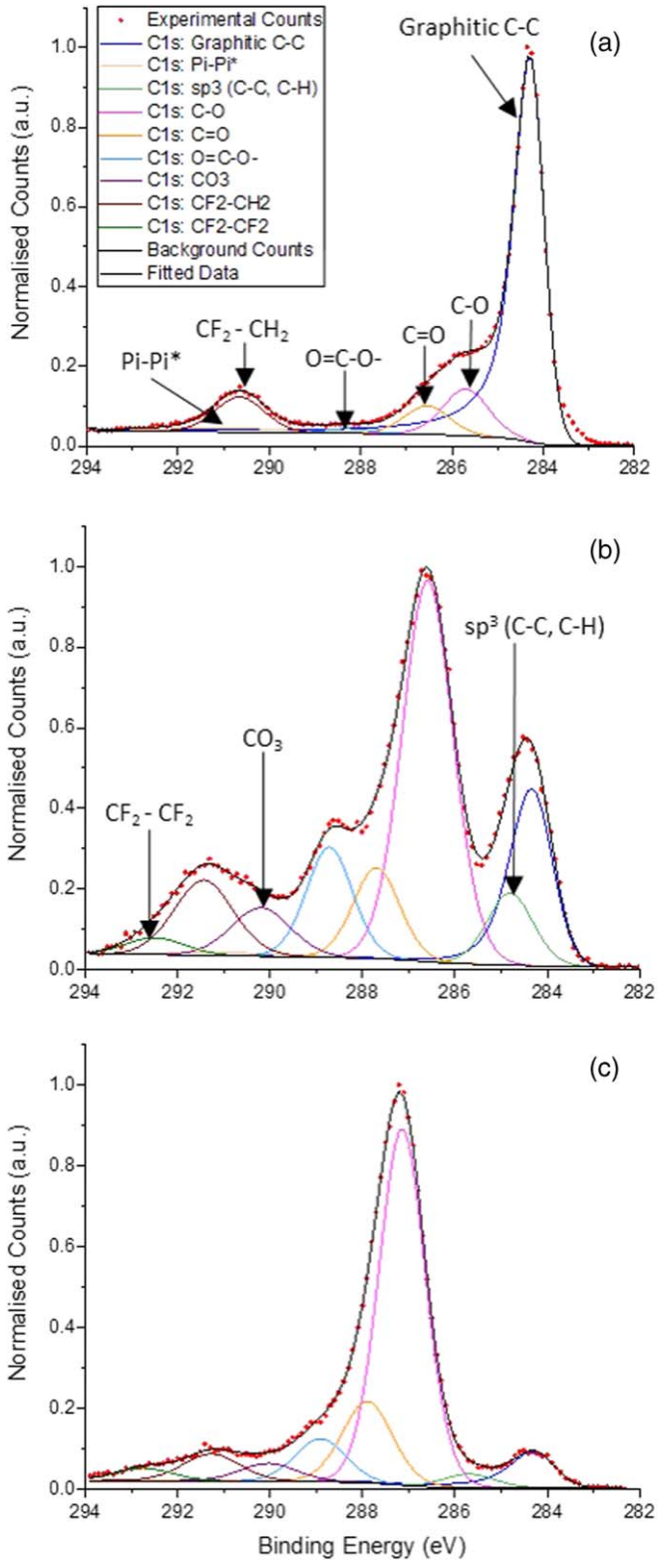


**Figure 14.** Anode XPS spectra of carbon C1s for (a) fresh, (b) standard formation and (c) case 2 (4 V–3.65 V) anodes after 500 cycles.

The O 1*s* spectrum (figure S.7 in supplementary information) of the fresh anode shows about 2.5% of total surface as oxygen presumably adsorbed on the surface during storage.

This value goes up to 12% in case 2 and up to above 20% in the standard formation anode, as shown in table 4. In all cases, the oxygen spectra were formed of various C–O and C=O bonds and trace amounts of moisture. As was the case in carbon species, this is a result of the electrolyte reduction. The increased amounts of oxygen in the standard formation case 1 suggests that having higher amounts oxygen may be affecting the cell performance. Trace amounts of water were observed on the fresh anode, which could have been absorbed on the

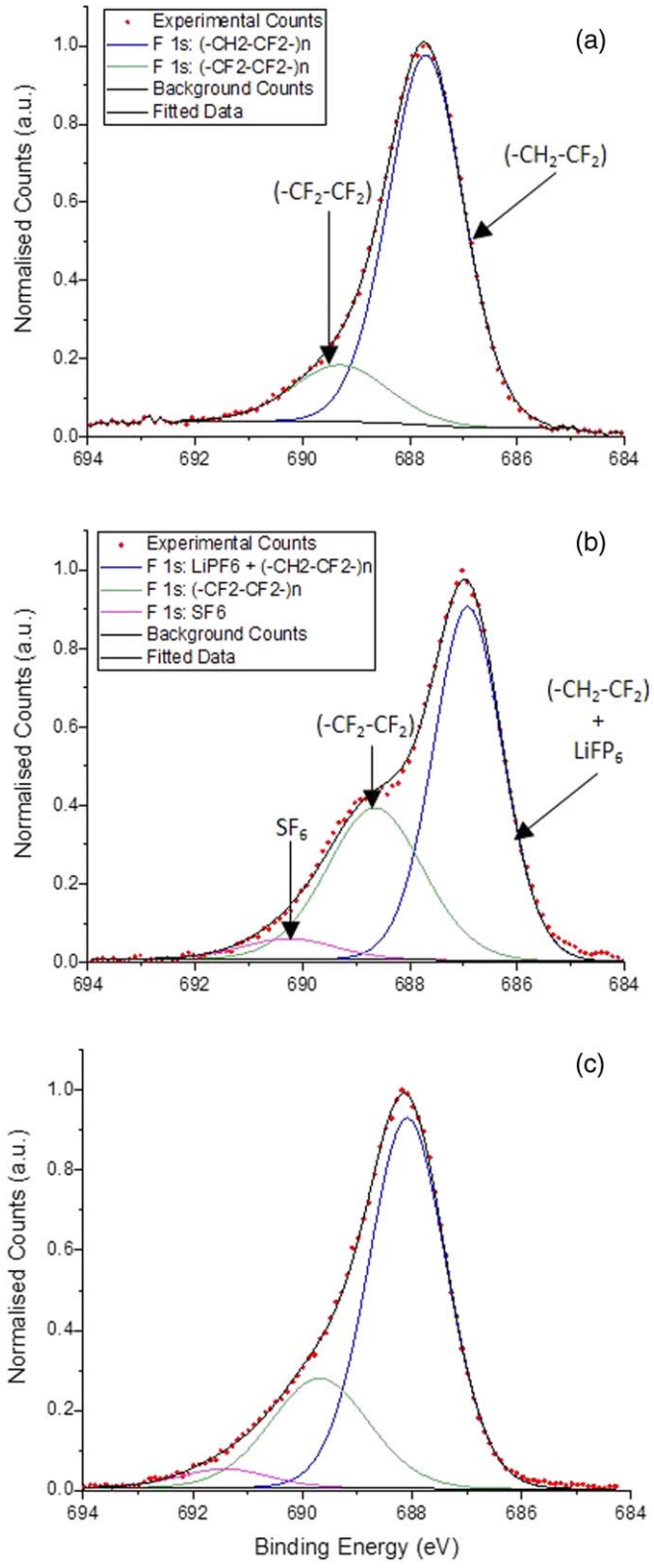


**Figure 15.** Anode XPS spectra of fluorine F1s for (a) fresh, (b) standard formation and (c) case 2 (4–3.65 V) anodes after 500 cycles.

surface during storage. This rises to just above 2% of the total surface in both cycled anodes and this higher proportion of moisture is likely coming from the electrolyte itself.

*3.2.1.2. Cathodes*

The XPS spectra of the fresh cathode had nickel, manganese, cobalt, lithium and oxygen peaks expected from a NMC-111 electrode (figure 16). The level of oxides was very low (only ~3.5% of the total surface) and only ~1% of the total surface was present as C–O bond. ~14% fluorine is present from the PVDF binder. Almost three

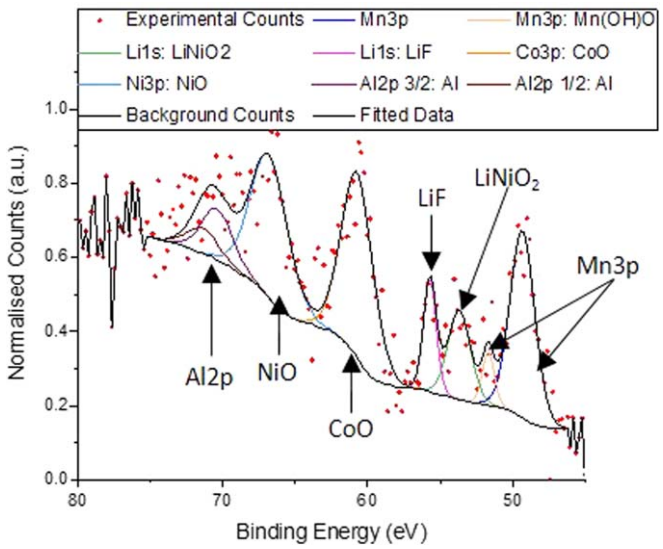


**Figure 16.** Cathode XPS spectrum of lithium and the transition metals for a fresh cathode.

**Table 5.** Elemental composition with bonding (in percentage) for cathodes obtained from XPS analysis for the fresh, and after 500 cycles for the standard formation and case 2 (4—3.65 V) cathodes.

| Element | Fluorine 1s | | | | Oxygen 1s | | | | | Carbon 1s | | | | | | | | Mangan ese 3p | | Lithium 1s | | Cobalt | Nickel | Alumini um 2p | | | Silicon 2p | | Phosphorous 2p | | | | Sulphur 2p | |
|---|---|---|---|---|---|---|---|---|---|---|---|---|---|---|---|---|---|---|---|---|---|---|---|---|---|---|---|---|---|---|---|---|---|
| Bonding | LiF | LiPF6+(-CH2- | (-CF2-CF2-)n | SF6 | NiO | M-(OH)x | C-O-C (Aliphatic) | O-(C=O)-C | H2O | Graphitic C-C | Pi-Pi* | sp3 (C-C, C-H) | C-O | C=O | O=C--O- | CO3 | CF2-CH2 | CF2 | Mn | Mn(OH)O | LiNiO2 | LiF | CoO | NiO | Al2p 3/2 | Al2p ½ | Al2O3 | Si 2p 3/2: SiOx/Si | Si 2p 1/2: SiOx/Si | P 2p3/2: PO4 | P 2p1/2: PO4 | P 2p3/2: PF6 | P 2p1/2: PF6 | S 2p 3/2: M(SO4) | S 2p 1/2: M(S)4) |
| Fresh Cathode | - | 14.25 (-CH2-CF2- | 1.21 | - | 0.95 | 2.45 | 0.95 | - | - | 42.08 | 2.11 | 12.56 | 10.85 | 1.70 | 1.57 | - | 5.58 | - | 0.15 | 0.02 | 1.67 | 1.22 | 0.14 | 0.12 | 0.22 | 0.21 | - | - | - | - | - | - | - | - |
| Standard Formation | 9.20 | 15.43 | 0.89 | - | 1.06 | 2.22 | 4.92 | 3.54 | 0.60 | 19.62 | 0.98 | 6.58 | 4.82 | 1.90 | 1.88 | 1.26 | 2.52 | 0.33 | 0.23 | 0.08 | 9.07 | 5.94 | 0.22 | 0.22 | 1.87 | 1.84 | 0.64 | 0.49 | 0.48 | 0.30 | 0.15 | 0.29 | 0.14 | 0.20 | 0.10 |
| Case 2 (4 – 3.65 | 9.25 | 19.90 | 2.08 | 2.51 | 0.77 | 1.67 | 4.40 | 3.22 | 0.29 | 14.34 | 0.72 | 9.47 | 3.79 | 1.59 | 2.68 | - | 2.32 | - | 0.16 | 0.06 | 9.12 | 7.26 | 0.31 | 0.12 | 0.18 | 0.18 | - | 0.77 | 0.76 | 0.41 | 0.20 | 0.84 | 0.42 | 0.14 | 0.07 |

quarters of the area was detected as carbon. Trace levels of aluminium were detected that would have originated from the metal foil exposed during the sample preparations.

In the case of the cycled electrodes, an increased level of oxygen was detected with 0.5% water (from the electrolyte, as seen in the anodes). In addition to this, electrolyte degradation products were found on the cycled cathodes. Table 5 shows the elemental composition in percentage for all the elements and their bonding present in a fresh, standard formation and the case 2 (4 V–3.65 V) cathode samples (figures S.8–S.10 in supplementary information).

Figure 17 shows the C1s spectra from the three cathodes. The fresh cathode shows a significant graphitic carbon peak at 284.3 eV coming from the KS 6L conductive graphite and trace amounts of hydrocarbon bonding environments. ~7% of the total carbon was present as C–F bonds arising from PVDF binder. After cycling for 500 cycles, the graphite peak intensity decreases in both the standard formation and case 2 cathodes. The key feature difference in the standard formation and case 2 (4–3.65 V) cathodes was the presence of carbonates. As discussed with the anodes and the SEI layer, the higher levels of carbonates on the poor anode resulted in the degradation of the capacity of the cells. Similarly, in the case of poor cathodes, 1.24% of the total surface was

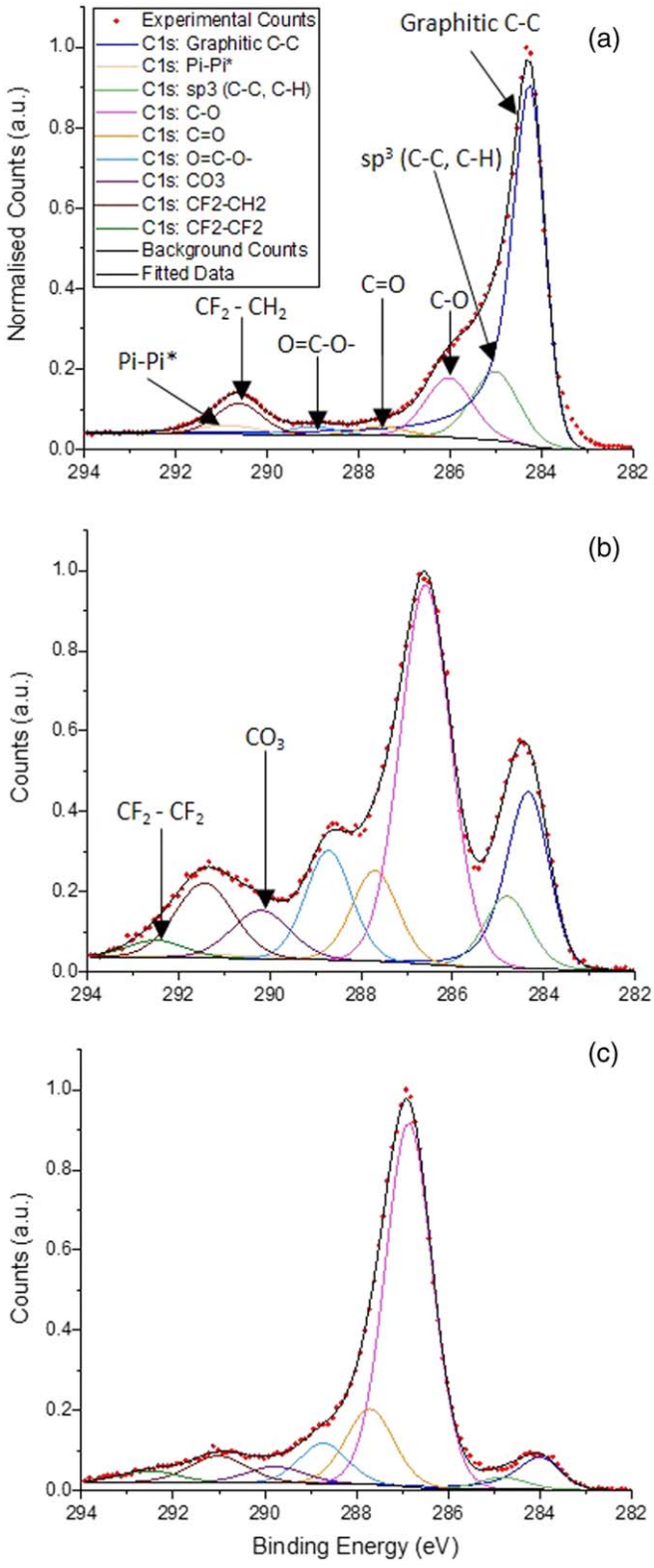


**Figure 17.** Cathode XPS spectra of carbon C1s for (a) fresh, (b) standard formation and (c) case 2 (4–3.65 V) cathodes after 500 cycles.

carbonates, as no carbonates were detected on the standard formation cathode and case 2 cathode, respectively; confirming the detrimental effects of carbonates on the battery cycle life. Furthermore, fluorinated PVDF was also found on the standard formation cathode, while no $(CF_2\text{-}CF_2)_n$ bonding was found on the case 2 cathode, as can be seen in figure 17. Interestingly, a large contribution to the surface fluorine was assigned to the likely formation of LiF on the surface after cycling. The sample, which did not undergo formation, showed a greater proportion of LiF on the cathode surface than the cell that underwent formation.

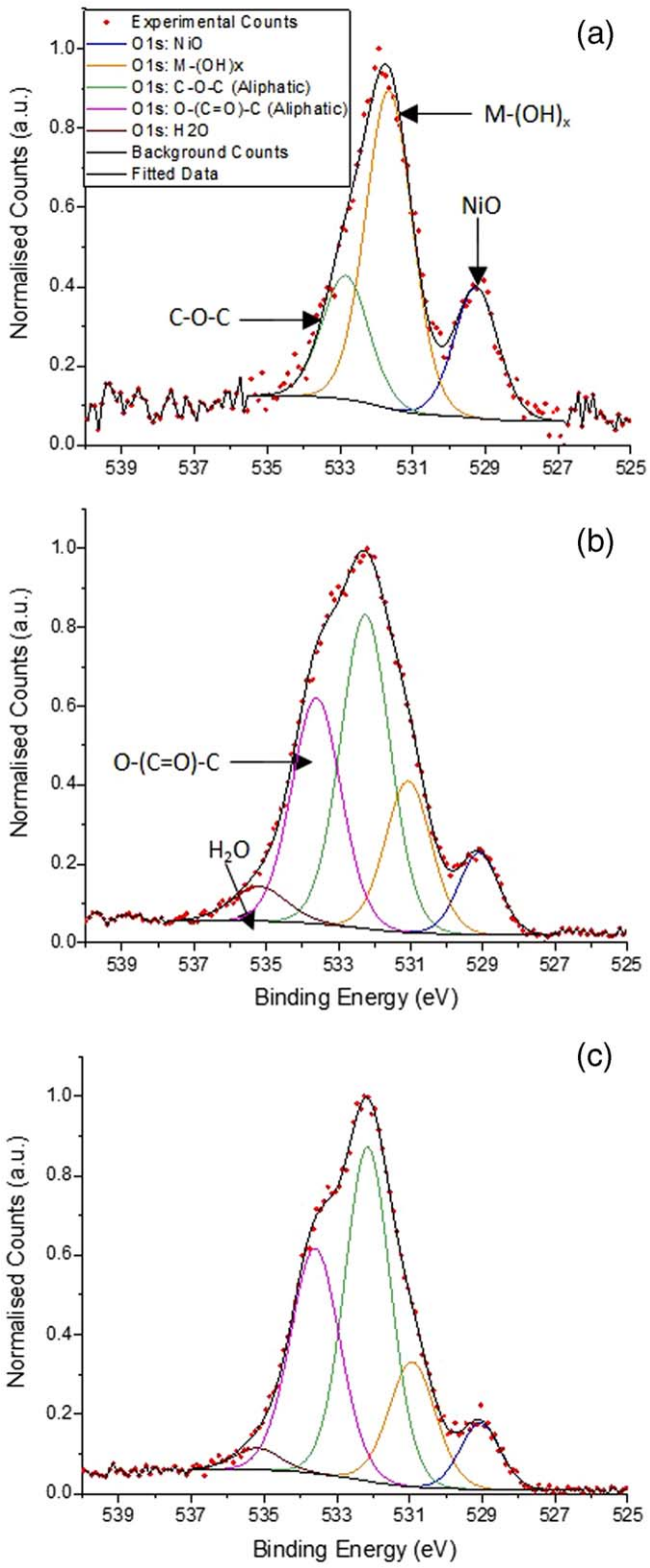


**Figure 18.** Cathode XPS spectra of oxygen O 1s for (a) fresh, (b) standard formation and (c) case 2 (4–3.65 V) cathodes after 500 cycles.

The O 1*s* spectrum of the fresh cathode shows just over 4% of the total surface as oxygen with over 3% coming from metal oxides. In the case of the cycled cathodes; both standard formation and case 2 cathodes, C–O–C and C=O bonds are present, which would be a result of the degradation of the electrolyte. In addition to this, similar to the cycled anodes, trace amounts of moisture were detected on both cathodes. Figure 18 shows the XPS spectra for the three cathodes.

Figure 19 shows the F1s spectra for the three cathodes. The F1s spectrum from the fresh cathode electrode showed $(CH_2\text{-}CF_2)_n$ bonding at 687.8 eV and $(CF_2\text{-}CF_2)_n$ at 689.2 eV for PVDF and fluorinated PVDF,

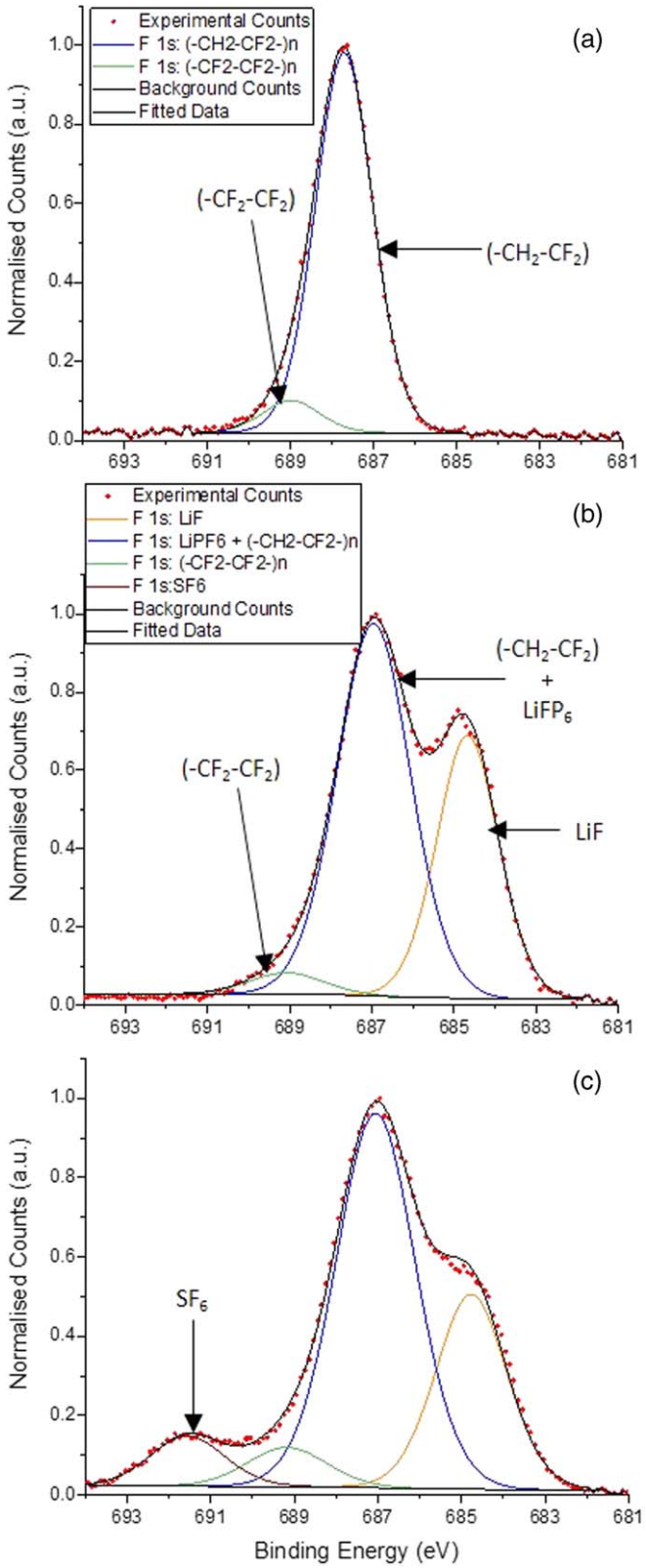


**Figure 19.** Cathode XPS spectra of fluorine F1s for (a) fresh, (b) standard formation and (c) case 2 (4–3.65 V) cathodes after 500 cycles.

respectively. The cycled cathodes were almost similar, with ~9% of the total surface being LiF. In addition to the PVDF binder peak, $LiPF_6$ was present on the cycled cathodes.

*3.2.2. SEM imaging*

In addition to the XPS analysis, SEM imaging was performed on the three cells of a given formation protocol case.

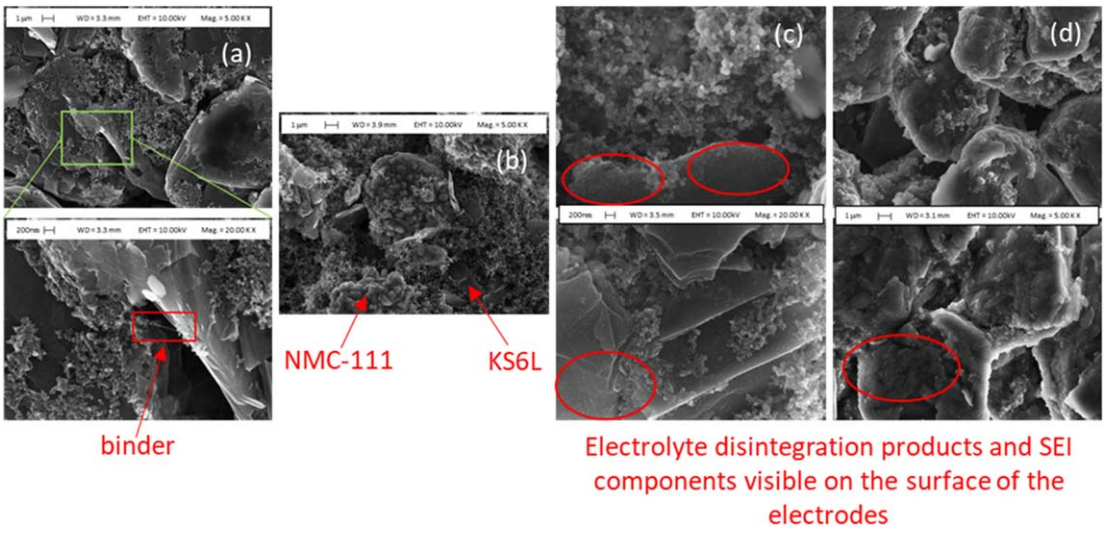


**Figure 20.** An SEM image of (a) the fresh anode at 5 k x magnification (top) and magnified image at 20 k x (bottom) of the green area. Area marked in red shows the binder in the anode, (b) the fresh cathode at 5 k x magnification, (c) the two cycled anodes at 5 k x magnification with the standard formation sample at the top and the case 2 (4–3.65 V) sample at the bottom and (d) the two cycled cathodes at 20 k x magnification with the standard formation sample at the top and the case 2 (4–3.65 V) sample at the bottom.

Figure 20(a) shows the SEM image of a fresh anode. The top image shows multiple flakes of graphite on top of each other surrounded by clusters of conductive carbon additive. The bottom image shows the magnified section from the top image marked in green. The red marked area in the magnified image shows the binder particle between the graphite and the conductive carbon. The SEM images correlate to the XPS data of fresh anodes with most of the sample being carbon, and fluorine from the PVDF binder.

Figure 20(b) shows the SEM image of a fresh cathode. The conductive additives demonstrate similar structure for the anodes, as can be seen in figure 20(a). The larger clusters or agglomerates formed of multiple smaller particles are those of the active material NMC-111. Conductive graphite flakes of KS 6L can also be seen in the image.

Figure 20(c) shows the SEM images for the cycled anodes after 500 cycles. In both the standard and case 2 samples, the surfaces are covered with deposits that were also evident in the XPS data. These deposits are the SEI layer and electrolyte degradation products. In addition, some of the salts from the electrolyte that would have been left behind after electrolyte evaporation would also be on the surface.

Comparing the cycled to the fresh graphite electrodes (figures 20(a) and (c)), it can be observed that there is a thin film that formed over the surface of the graphite in the cycled electrodes. The carbon additives also appear to be coated in this film, and it appears to be 'gluing' all the components together. Within the limitations of the image resolution available, it is very difficult to differentiate between the two SEI layers in the standard formation case 1 and case 2 (4 V–3.65 V) samples. However, in the images the case 2 anode seems to have a uniform cover on the surface as opposed to the non-uniform deposits in the standard formation anode.

## 4. Summary and conclusions

CR2032 coin cells made with NMC-111 versus graphite have been tested using various formation protocols in a laboratory maintained at 25 °C. The electrolyte used was 1.0 M $LiPF_6$ in EC/EMC = 3/7 (v/v) + 1%wt. VC. A range of voltage windows between 2.6–4.0 V were analysed to optimise the formation process. Capacity retention and increase in resistance over 500 cycles were analysed and optimum results were obtained for the formation that occurred at the higher voltage window (between 3.65–4.0 V).

The presented electrochemical and XPS data show that the cycling life and the capacity retention for NMC-111/graphite cells is strongly influenced by the nature and composition of the SEI layer. A stable, uniform, lithium-conductive and thin SEI layer is preferred to minimise any capacity loss due to resistance of the SEI film. An irregular and non-uniform SEI layer would result in continued SEI growth, and associated lithium loss results in quick capacity fade due to fresh graphite being exposed to the electrolyte, which would result in further electrolyte decomposition. This is illustrated by the decomposition compounds on the graphite surface. XPS shows that the composition of the SEI layer is directly influenced by the products formed as a result of the electrolyte decomposition that deposit on the surface of the anode. The higher proportion of carbonates in the anode of the unformed cell suggests that the presence of carbonates on the surface is detrimental to the cycle life

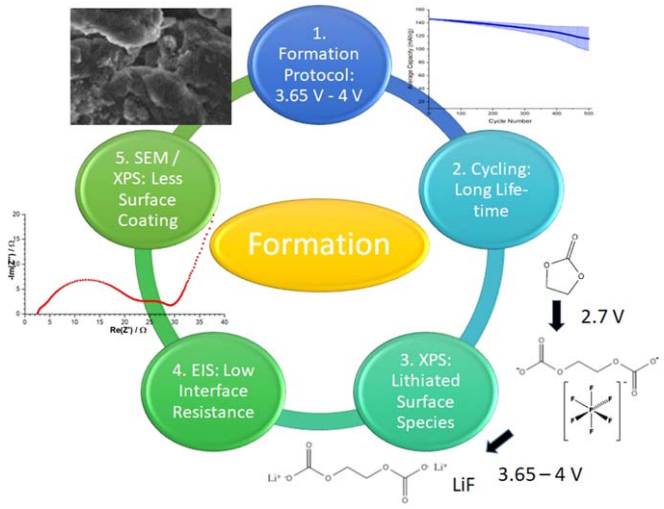


**Figure 21.** Summary of the results indicating the effects of formation upon the interfaces of the anode and cathode in the NMC-111 versus graphite lithium-ion cell.

of the cell. This is further confirmed with the absence of any carbonates on the cycled cathodes of the 'good' cell and trace amounts of carbonates on the 'poor' cathode. The fluorination of the PVDF binder also has an adverse effect on the cycling life of the cells. As the voltage is increased in a full-cell configuration, lithium is removed from the cathode and the lithium ions are transferred through the organic decomposition layer into the graphite. As the lithium ions move through the organic decomposition layer, they can then further react to form lithiated species within the SEI layer. Surprisingly, there was also a correlation with the CEI, with no formation a greater degree of LiF, and PTFE was observed on the surface.

The key conclusions are summarised in figure 21 and below:

1. Targeted voltage window cycling for an active formation has a positive effect upon the lifetime and cycling performance of a full cell; especially the voltage window at the higher voltages (>3.65 V).
2. Formation protocols are extremely important in order to maintain a good cycle life of an LIB.
3. Interface chemical species.
   a. The cathode showed also an effect of ageing and LiF, and $CF_2$-$CF_2$ were observed in the XPS analysis of the cycled electrodes, indicating a contribution from the CEI to poor cycling.
   b. Increase in the oxygen surface species in the cycled electrodes showed ether surface compounds, which is likely due to the breakdown of the electrolyte forming ethers and carbonyl oxygen bonding environments.
   c. Lithiated SEI layers are important towards a stable interface layer, and therefore the cell voltage window chosen is where the graphite voltage is close to 0 V versus Li/Li+ and the layered oxide voltage is $< 4.0$ V versus Li/Li+.
4. Impedance of the SEI after formation does not necessarily reflect the better cycling of the cells. However, the cases which showed improved cycle life showed the least increase in SEI resistance when compared with the ones obtained immediately after formation and after 500 cycles.
5. The impedance of the SEI grows with the number of cycles in all cases. However, a minimal increase is desirable, representing a stable SEI layer.

## Acknowledgments

The authors would like to acknowledge the Catapult funding and WMG, University of Warwick. The authors would also like to acknowledge Ryan Malcolmson, Mattea Said Conti, Michael Lain, Samuel Roberts, Dominika Gastol and Scott Gorman for their input at various stages of the manuscript.

## Conflicts of interest

The authors declare that there is no conflict of interest regarding the publication of this paper.

## ORCID iDs

Tanveerkhan S Pathan https://orcid.org/0000-0003-4192-5109
W D Widanage https://orcid.org/0000-0003-0428-2554
Emma Kendrick https://orcid.org/0000-0002-4219-964X

## References

[1] Mao C *et al* 2018 Balancing formation time and electrochemical performance of high energy *J. Power Sources* **402** 107–15
[2] An S J, Li J, Du Z, Daniel C and Wood D L 2017 Fast formation cycling for lithium ion batteries *J. Power Sources* **342** 846–52
[3] Long B R *et al* 2016 Enabling high-energy, high-voltage lithium-ion cells: standardization of coin-cell assembly, electrochemical testing, and evaluation of full cells *J. Electrochem. Soc.* **163** A2999–3009
[4] Myung S T *et al* 2017 Nickel-rich layered cathode materials for automotive lithium-ion batteries: achievements and perspectives *ACS Energy Lett.* **2** 196–223
[5] European Commission 2018 Reducing $CO_2$ emissions from passenger cars (https://ec.europa.eu/clima/policies/transport/vehicles/cars_en) (Accessed: 9 October 2018)
[6] Mao C *et al* 2018 Balancing formation time and electrochemical performance of high energy *J. Power Sources* **402** 107–15
[7] Liu J *et al* 2019 Pathways for practical high-energy long-cycling lithium metal batteries *Nat. Energy* **4** 180–6
[8] Wang H-G, Yuan S, Ma D-L, Zhang X-B and Yan J-M 2015 Electrospun materials for lithium and sodium rechargeable batteries: from structure evolution to electrochemical performance *Energy Environ. Sci.* **8** 1660–81
[9] Li J *et al* 2017 Toward low-cost, high-energy density, and high-power density lithium-ion batteries *JOM* **69** 1484–96
[10] Trask S E *et al* 2014 From coin cells to 400 mAh pouch cells: Enhancing performance of high-capacity lithium-ion cells via modifications in electrode constitution and fabrication *J. Power Sources* **259** 233–44
[11] Meister P, Jia H, Li J, Kloepsch R, Winter M and Placke T 2016 Best practice: performance and cost evaluation of lithium ion battery active materials with special emphasis on energy efficiency *Chem. Mater.* **28** 7203–17
[12] Radin M D *et al* 2017 Narrowing the gap between theoretical and practical capacities in li-ion layered oxide cathode materials *Adv. Energy Mater.* **7** 1–33
[13] Kendrick E 2019 Advancements in manufacturing *Future Lithium-ion Batteries* ed A Eftekhari (London: The Royal Society of Chemistry) pp 262–89
[14] Roberts S and Kendrick E 2018 The re-emergence of sodium ion batteries : testing, processing, and manufacturability *Nanotechnol. Sci. Appl.* **11** 23–33
[15] Wood D L, Li J and Daniel C 2015 Prospects for reducing the processing cost of lithium ion batteries *J. Power Sources* **275** 234–42
[16] Nie M, Chalasani D, Abraham D P, Chen Y, Bose A and Lucht B L 2013 Lithium ion battery graphite solid electrolyte interphase revealed by microscopy and spectroscopy *J. Phys. Chem.* C **117** 1257–67
[17] Peled E and Menkin S 2017 Review—SEI: past, present and future *J. Electrochem. Soc.* **164** A1703–19
[18] Ramasubramanian A, Yurkiv V, Foroozan T, Ragone M, Shahbazian-Yassar R and Mashayek F 2019 Lithium diffusion mechanism through solid-electrolyte interphase in rechargeable lithium batteries *J. Phys. Chem.* C **123** 10237–45
[19] Vissers D R *et al* 2016 Role of manganese deposition on graphite in the capacity fading of lithium ion batteries *ACS Appl. Mater. Interfaces* **8** 14244–51
[20] Glazier S L, Li J, Louli A J, Allen J P and Dahn J R 2017 An analysis of artificial and natural graphite in lithium ion pouch cells using ultra-high precision coulometry, isothermal microcalorimetry, gas evolution, long term cycling and pressure measurements *J. Electrochem. Soc.* **164** A3545–55
[21] Gilbert J A *et al* 2017 Cycling behavior of NCM523/graphite lithium-ion cells in the 3–4.4 V range: diagnostic studies of full cells and harvested electrodes *J. Electrochem. Soc.* **164** A6054–65
[22] Agubra V A and Fergus J W 2014 The formation and stability of the solid electrolyte interface on the graphite anode *J. Power Sources* **268** 153–62
[23] Balbuena P B and Wang Y (ed) 2007 *Lithium-Ion Batteries: Solid Electrolyte Interphase* (London: Imperial College Press)
[24] Chang C C, Wu C-M, Ho G-T, Chen H-Y, Pan P-I and Fung K-Z 2019 Thickness evaluation of solid electrolyte interphase layer and lithium diffusion phenomenon on negative electrodes for li-ion batteries by neutron scattering study *Meet. Abstr.* **MA2019-03** 135
[25] Kumatani A, Sato Y, Takahashi Y, Shiku H and Matsue T 2019 Scanning electrochemical cell microscopy for analysis of solid electrolyte interface on negative electrodes in lithium-ion batteries *Meet. Abstr.* **MA2019-01** 2267
[26] Liu T *et al* 2019 *In situ* quantification of interphasial chemistry in Li-ion battery *Nat. Nanotechnol.* **14** 50–6
[27] Eshetu G G *et al* 2019 Impact of the electrolyte salt anion on the solid electrolyte interphase formation in sodium ion batteries *Nano Energy* **55** 327–40
[28] Moulder J F, Stickle W F, Sobol P E and Bomben K D 1992 Handbook of x-ray photoelectron spectroscopy ed J Chastain *Physical Electronics, Inc.* (Waltham, MA: Perkin-Elmer Corporation)
[29] An S J, Li J, Daniel C, Mohanty D, Nagpure S and Wood D L 2016 The state of understanding of the lithium-ion-battery graphite solid electrolyte interphase (SEI) and its relationship to formation cycling *Carbon N Y* **105** 52–76
[30] Levi M D and Aurbach D 1997 Simultaneous measurements and modeling of the electrochemical impedance and the cyclic voltammetric characteristics of graphite electrodes doped with lithium *J. Phys. Chem.* B **101** 4630–40
[31] Aurbach D, Markovsky B, Weissman I, Levi E and Ein-eli Y 1999 On the correlation between surface chemistry and performance of graphite negative electrodes for Li ion batteries *Electrochim. Acta* **45** 67–86